

GET-UP: GEomeTric-aware Depth Estimation with Radar Points UPsampling

Huawei Sun^{1,2}, Zixu Wang^{1,2}, Hao Feng¹, Julius Ott^{1,2}, Lorenzo Servadei¹, Robert Wille¹

¹ Technical University of Munich, Munich, Germany

² Infineon Technologies AG, Neubiberg, Germany

Abstract

Depth estimation plays a pivotal role in autonomous driving, facilitating a comprehensive understanding of the vehicle’s 3D surroundings. Radar, with its robustness to adverse weather conditions and capability to measure distances, has drawn significant interest for radar-camera depth estimation. However, existing algorithms process the inherently noisy and sparse radar data by projecting 3D points onto the image plane for pixel-level feature extraction, overlooking the valuable geometric information contained within the radar point cloud. To address this gap, we propose GET-UP, leveraging attention-enhanced Graph Neural Networks (GNN) to exchange and aggregate both 2D and 3D information from radar data. This approach effectively enriches the feature representation by incorporating spatial relationships compared to traditional methods that rely only on 2D feature extraction. Furthermore, we incorporate a point cloud upsampling task to densify the radar point cloud, rectify point positions, and derive additional 3D features under the guidance of lidar data. Finally, we fuse radar and camera features during the decoding phase for depth estimation. We benchmark our proposed GET-UP on the nuScenes dataset, achieving state-of-the-art performance with a 15.3% and 14.7% improvement in MAE and RMSE over the previously best-performing model. Code: <https://github.com/harborsarah/GET-UP>

1. Introduction

Understanding the 3D environment surrounding the ego vehicle is essential in the autonomous driving field, requiring the estimation of dense depth maps for 3D scene reconstruction. While learning-based monocular depth estimation methods [1, 6, 9, 12, 19, 22, 32] have outperformed traditional monocular-based approaches [35, 36, 46] in accuracy, they are still constrained by the lack of robust geometric constraints. To address this limitation, methods [7, 10, 15, 28, 30, 34, 42, 50] leveraging both depth sensors (i.e. LiDAR) and RGB images to first project LiDAR points

onto the image plane, resulting in a sparse depth map. However, these methods require additional tasks such as surface normal estimation for improved feature learning [34].



Figure 1. Visualization of projected radar points compared with the selected LiDAR points employed for point cloud upsampling.

Although LiDAR provides detailed information about 3D scenes, it is prohibitively expensive and sensitive to weather conditions. In contrast, radar offers robust performance in all weather conditions and is more cost-effective than LiDAR. However, the absence of height information in radar data and noisy characteristics lead to significant errors when projecting radar points onto the image plane. To illustrate how this discrepancy complicates depth estimation, we analyzed the absolute depth differences between each radar point and its nearest corresponding LiDAR point on the 2D image plane across the dataset. As shown in Figure 2, the depth values associated with radar points frequently deviate significantly from those of LiDAR, which serves as the ground truth. This discrepancy highlights why LiDAR-camera depth completion algorithms, which typically propagate depth information from LiDAR points to surrounding pixels, are ill-suited for radar-camera setups, indicating that radar-specific algorithms need to be developed.

Studies like [3, 16] directly project radar points onto the image plane, resulting in sparse and ambiguous radar projection maps. Others extend the height of each radar point [24, 29, 39, 41] or adopt two-stage processes producing semi-dense radar depth maps [26, 37, 40] to mitigate this issue. However, these methods often distort 3D geometric details, thereby limiting feature extraction in 2D space and introducing further noises into the radar data by directly altering the radar input.

To address these challenges, we propose GET-UP, a novel radar-camera depth estimation framework that uti-

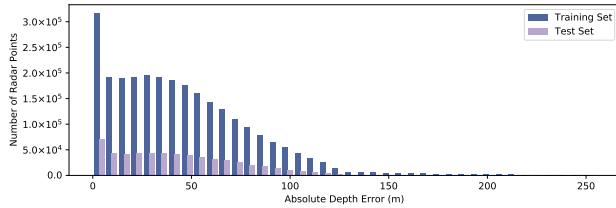


Figure 2. Absolute depth difference between each radar point and its corresponding nearest LiDAR point.

lizes radar input across two domains. Firstly, the 3D radar points are projected onto the image plane and densified by proposed Adaptive Sparse Convolution Block (ASCB), followed by ResNet-18 [13], yielding 2D radar features. Secondly, we employ an attention-enhanced Dynamic Graph Convolutional Neural Network (DGCNN) to capture 3D information and facilitate interaction with 2D features.

A key contribution of our method is the incorporation of point cloud upsampling as an auxiliary task. This block refines the radar features from precise LiDAR data, addressing the inherent ambiguity problem in radar point positions and ensuring that the densification process does not introduce extraneous noise into the radar inputs. Since the depth ground truth is generated from LiDAR data, no additional resource is needed for this training process. Figure 1 visualizes the radar and selected LiDAR points projections, serving as the ground truth for the upsampling task. To the best of our knowledge, our work is the first radar-camera depth estimation method to explicitly consider the 3D geometric information in radar point clouds. Moreover, this study pioneers using a point cloud upsampling strategy to effectively address the challenge of radar data sparsity. In summary, our principal contributions are:

- A novel depth estimation framework is proposed that uniquely takes advantage of 2D and 3D representations of radar data.
- An attention-enhanced DGCNN model is designed to adeptly extract 3D features while preserving the integrity of 2D spatial information.
- We present two innovative and effective approaches to address radar data sparsity: the ASCB for improving feature extraction in the 2D space and a dedicated point cloud upsampling task for enriched radar point representation from the 3D perspective.
- Our GET-UP model outperforms existing state-of-the-art radar-camera depth estimation techniques on the nuScenes dataset [2].

2. Related Work

Geometry-aware Depth Completion. Initial studies in LiDAR-camera depth completion [7, 15, 28, 30, 42, 50] predominantly perform depth completion within the 2D image plane by projecting sparse LiDAR points onto it, which fall short of capturing the underlying 3D geometric information. Instead, the following studies also extract features from the

3D perspective. Xiong *et al.* [49] employ a GNN by treating each image pixel as a graph node and establishing connections based on the k-Nearest-Neighbor (kNN) principle in 3D space. Further advancements include graph propagation techniques as seen in [53], enhancing multi-modal feature integration. Moreover, Point-Fusion [14], FuseNet [5], and [52] extract 3D features from 3D LiDAR points and consolidate 2D and 3D features.

Nevertheless, these approaches are constrained by relying on a predefined number of LiDAR points as input, which cannot handle the various number of radar points.

Radar-Camera Depth Estimation. Radar point clouds are significantly sparser and noisier than LiDAR, presenting a challenge for generating dense depth maps from images and radar data. Lin *et al.* [23] directly project radar points onto the image plane, yielding highly-sparse and ambiguous radar maps. To mitigate the sparsity issue, [20, 24] extend radar points vertically, creating denser radar projection maps. Differing from direct radar-to-image projection, [26, 37, 40] propose two-stage architectures that explore one-to-many mapping from radar data to image pixels in the first stage, producing denser intermediate radar data for subsequent depth prediction.

However, the densify processes in the existing studies introduce further noises into the radar data since they directly modify the radar input. Furthermore, the projection process overlooks the 3D geometric information of radar data.

Point Cloud Upsampling. Point cloud upsampling is a typical task for point cloud densification, which is designed to transform sparse and noisy point clouds into denser and cleaner counterparts [8, 21, 27, 33, 51]. This procedure typically begins with extracting point features, followed by point expansion and coordinate reconstruction, a methodology initially introduced by PU-Net [51]. Subsequently, PU-GAN [21] innovated by incorporating an adversarial network to optimize point distribution. Further, GNNs are utilized in PU-GCN [33] for both feature extraction and expansion phases to improve point cloud quality. Du *et al.* [8] advances by introducing a cascaded refinement network that employs a residual learning approach for incremental improvements. Nevertheless, point cloud upsampling task has not been used by existing radar-camera depth estimation methods to mitigate the radar point sparsity problem.

In this study, diverging from conventional radar-camera depth estimation techniques, which distort 3D geometric clues, we advance feature extraction by considering both 2D radar projection maps and 3D radar points. To address the challenges of sparsity and ambiguity inherent in radar point clouds, we are the first to introduce a point cloud upsampling module into the depth estimation task. This module, distinctively utilizing existing LiDAR points as ground truth, aims to both densify the radar data and enhance the precision of radar point positioning.

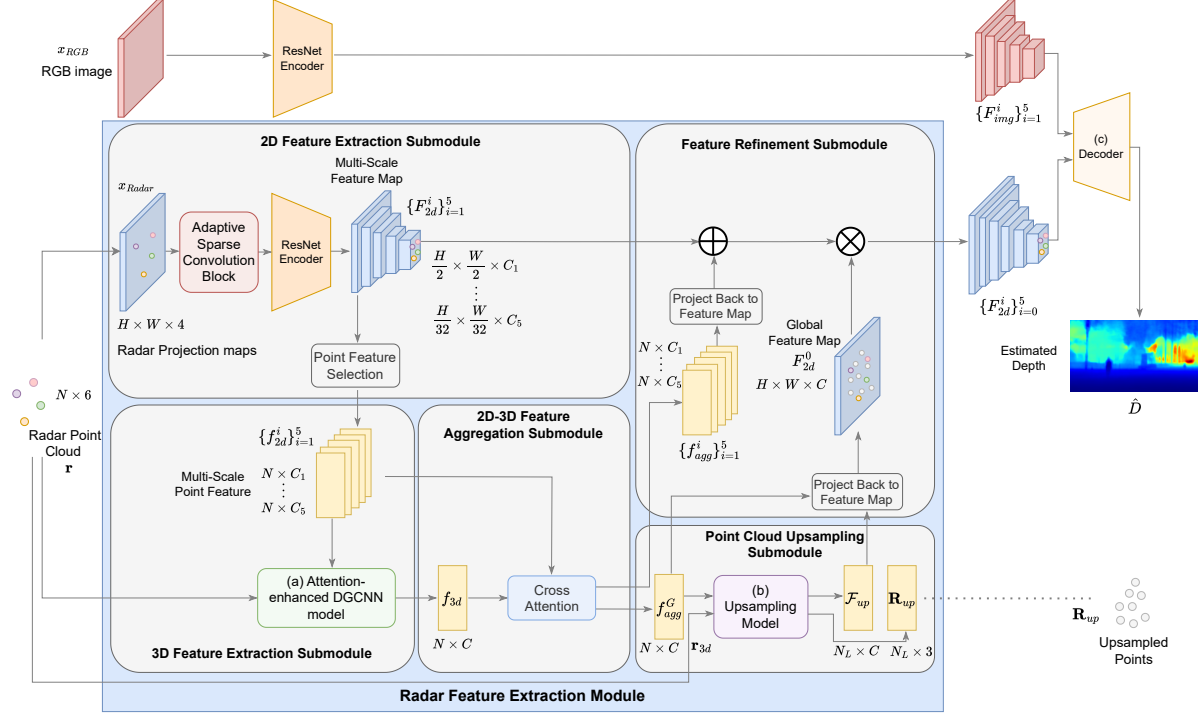


Figure 3. Model Architecture: The input image is processed through a ResNet encoder to extract features. Concurrently, radar data are processed by a specially designed radar feature extraction module, comprising five submodules, to yield refined radar features and upsampled points. These radar and image features are then integrated within the decoder to produce the estimated dense depth map. Detailed illustrations of the blocks (a), (b), and (c) are provided in Fig. 4, 5, and 6, respectively.

3. Approach

This section introduces the innovations of our work. In Sec. 3.1, we explain the model architecture. Subsequently, our proposed radar feature extraction module, including five submodules, is described in Sec. 3.2. Finally, we present our decoder of the depth estimation task in Sec. 3.3.

3.1. Model Architecture

As visualized in Figure 3, our model processes two key inputs: an image $x_{RGB} \in \mathbb{R}^{H \times W \times 3}$ and a radar point cloud $\mathbf{r} \in \mathbb{R}^{N \times C_r}$, where N denotes the number of radar points in the current frame and C_r is the number of features carried by the radar. Radar projection map $x_{Radar} \in \mathbb{R}^{H \times W \times C_R}$ is generated by projecting these N points onto the image plane, carrying specific attributes such as depth, velocities, and Radar Cross Section (RCS). Additionally, the point cloud \mathbf{r} encompasses 3D positional data.

The RGB image x_{RGB} is processed through a ResNet-34 encoder [13], yielding multi-scale features $\{F_{img}^i\}_{i=1}^5$. Concurrently, x_{Radar} and \mathbf{r} are processed by a dedicated radar feature extraction module, designed to extract coherent radar features by aggregating 2D and 3D information with five submodules. Notably, it includes a point cloud upsampling submodule aimed at leveraging precise LiDAR point positions to adjust and densify radar point represen-

tations. This submodule efficiently extracts features reflective of LiDAR positions, which are then used to enhance the radar-derived features. The output of this radar feature extraction process is a set of refined radar features $\{F_{2d}^i\}_{i=0}^5$, including a generated feature F_{2d}^0 with the same size as the input image, and an upsampled 3D point cloud \mathbf{R}_{up} . Sec. 3.2 provides a more detailed explanation of this process.

These processed image and radar features are subsequently fused through a gated fusion mechanism [37] and then fed into a depth estimation model [19]. This final step produces a comprehensive dense depth map $\hat{D} \in \mathbb{R}^{H \times W}$. More details are available in Sec. 3.3.

3.2. Radar Feature Extraction Module

The radar feature extraction module comprises five distinct submodules with x_{Radar} and \mathbf{r} as inputs. Initially, the *2D feature extraction submodule* processes x_{Radar} to generate multi-scale feature maps. Subsequently, these maps, jointly with \mathbf{r} , are input into the *3D feature extraction submodule*, to distill 3D geometry-aware features. Afterwards, the *2D-3D feature aggregation submodule* processed the 2D and 3D features, yielding enhanced and more reliable 3D feature representations. The obtained 3D features, integrated with \mathbf{r} , undergo further enhancement in the *point cloud upsampling submodule* to increase data density and precision. Lastly, a *feature refinement submodule* is em-

ployed to precisely refine the radar features, leveraging both the 2D spatial and 3D geometric information to obtain a comprehensive feature representation.

3.2.1 2D feature extraction submodule.

We introduce ASCB with sparse convolution layers [43] to address the challenge of highly sparse radar projections. This component adaptively adjusts the convolution kernel size based on the depth information of radar points. Initially, x_{Radar} undergoes processing by the ASCB, followed by a ResNet-18 backbone to further refine the ASCB output, yielding five feature sets $\{F_{2d}^i\}_{i=1}^5$ across different scales i , with each set $F_{2d}^i \in \mathbb{R}^{\frac{H}{2^i} \times \frac{W}{2^i} \times C_i}$. Suppose the radar point cloud comprising N points, where $\mathbf{r}_{2d} = \{(x_{2d}^j, y_{2d}^j)\}_{j=1}^N$ represent j^{th} point's projected pixel coordinate. Both these coordinates and the aforementioned multi-scale features are inputs to the point feature selection block.

Adaptive sparse convolution block. The Sparse Convolutional Network [43] utilizes an observation mask in each sparse convolutional layer to filter out “unobserved” pixels from the input during the convolution. However, objects that are farther away from the ego-vehicle appear smaller on the image plane. This leads to a challenge that it may upsample the projected points into a wrong scale, since all points are treated equally by a single mask.

Therefore, we propose the ASCB, which employs three binary observation masks to categorize radar detections by distance. Then, different convolution kernel sizes are selected for each group to enable precise feature propagation across different area sizes. Following a general statistical analysis of the projection size of common objects within our dataset, we select three distance range groups: $[0, 40)$, $[40, 70)$, and $[70, +\infty)$ meters. Within each range, a list of sparse convolutional layers with stride 1 is stacked to encode the input radar map according to the respective radar observation mask. We finally select the list of symmetric kernel sizes with $[11, 7, 7, 5, 5, 3]$, $[11, 7, 5, 5, 3, 3]$, and $[11, 7, 5, 3]$ for the aforementioned three distance groups. The outputs of these three ranges are element-wise summed to generate the final output of this block. The detailed experiments are introduced in the supplementary material.

Point feature selection. After obtaining the multi-scale feature maps, we select the 2D features of each point at different scales. Thus, this block involves scaling the pixel coordinates according to the feature map's scale factor. At scale i , point features are extracted at the coordinates $(\lfloor \frac{x_{2d}^j}{2^i} \rfloor, \lfloor \frac{y_{2d}^j}{2^i} \rfloor)$, yielding a set of five point feature vectors $\{f_{2d}^i\}_{i=1}^5$, with $f_{2d}^i \in \mathbb{R}^{N \times C_i}$.

3.2.2 3D feature extraction submodule.

As illustrated in Figure 4, our graph model effectively incorporates five EdgeConv blocks [47], where the graph is

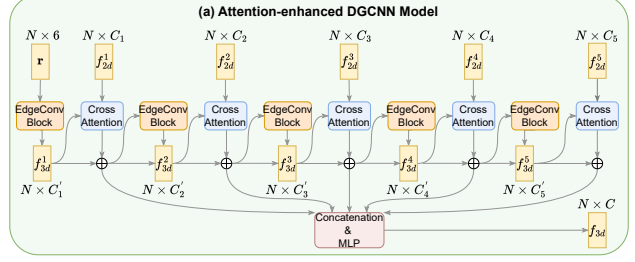


Figure 4. Proposed attention-based DGCNN model, which incorporates extracted 2D features during the 3D feature generation, resulting in a robust representation of 3D radar features derived from sparse and noisy radar point clouds.

constructed dynamically based on the kNN at each layer. This model aims to extract 3D point features from the input $\mathbf{r} = \{(x_{3d}^j, y_{3d}^j, z_{3d}^j, v_x^j, v_y^j, rcs^j)\}_{j=1}^N$, where the j^{th} point is located at $(x_{3d}^j, y_{3d}^j, z_{3d}^j)$ in 3D space. The output of the first EdgeConv block $f_{3d}^1 \in \mathbb{R}^{N \times C_1}$, alongside f_{2d}^1 , are input into a cross-attention block [45], with f_{3d}^1 acting as the query and f_{2d}^1 generating the keys and values. We also add skip connection after the cross-attention to mitigate the potential gradient vanishing issue, resulting in the refined feature $f_{3d}^{1'} \in \mathbb{R}^{N \times C_1}$

$$f_{3d}^{i'} = \text{Attention}(f_{3d}^i W_{3dQ}^i, f_{2d}^i W_{3dK}^i, f_{2d}^i W_{3dV}^i) + f_{3d}^i. \quad (1)$$

Subsequently, $f_{3d}^{1'}$ progresses to the next EdgeConv block. We repeat the EdgeCov block and cross-attention five times, yielding five intermediate features $\{f_{3d}^{i'}\}_{i=1}^5$, and they are further concatenated along the channel dimension processed by following MLP layers to generate the final feature output $f_{3d} \in \mathbb{R}^{N \times C}$.

3.2.3 2D-3D feature aggregation submodule.

With f_{3d} from the 3D feature extraction module and a set of 2D point features $\{f_{2d}^i\}_{i=1}^5$ at various scales i from the 2D feature extraction module, the cross-attention operation uses f_{3d} as the query and f_{2d}^i as both key and value, yielding five aggregated features $\{f_{agg}^i\}_{i=1}^5$, each matching the dimensions of f_{2d}^i

$$f_{agg}^i = \text{Attention}(f_{3d} W_{aggQ}^i, f_{2d}^i W_{aggK}^i, f_{2d}^i W_{aggV}^i). \quad (2)$$

Furthermore, to derive a comprehensive global aggregated feature that spans all scales, the 2D features are concatenated across the channel dimension, and further apply cross-attention between this concatenated 2D feature and f_{3d} , resulting in a global aggregated feature $f_{agg}^G \in \mathbb{R}^{N \times C}$

$$f_{agg}^G = f_{2d}^1 \otimes f_{2d}^2 \otimes f_{2d}^3 \otimes f_{2d}^4 \otimes f_{2d}^5 \\ f_{agg}^G = \text{Attention}(f_{3d} W_{aggQ}^G, f_{agg}^G W_{aggK}^G, f_{agg}^G W_{aggV}^G), \quad (3)$$

where \otimes signifies the concatenation of features along the channel dimension.

3.2.4 Point cloud upsampling submodule.

As a key module of GET-UP, we enhance radar data quality by leveraging the precision of LiDAR data, aiming to accurately identify and rectify the positioning of radar points. We start by detailing the approach for generating ground truth data, followed by the upsampling model architecture.

Ground truth generation. Given the significant sparsity difference between LiDAR and radar point clouds—with radar detections being up to $1000\times$ sparser per frame [2]—it is impractical to use the entire LiDAR dataset as ground truth for upsampling. Instead, a subset of N_L LiDAR points is selected for ground truth supervision. A naive approach is randomly sampling these N_L points from the LiDAR point cloud. However, this method fails to account for the spatial relevance of LiDAR points to actual radar detections. To address this, we refine our selection process by first calculating the Chamfer distance [11] between radar and LiDAR points, then prioritize the N_L LiDAR points with the smallest distances, effectively choosing those closest to the radar points as the upsampling ground truth \mathbf{R}_{gt} .

Upsampling model architecture. Similar to existing methodologies [8, 33], our approach focuses on learning the offsets of target points rather than directly predicting their 3D positions. Nevertheless, unlike the typical point cloud upsampling task, we encounter the challenge that the quantity of radar points varies from frame to frame, resulting in an unpredictable upsampling ratio across different frames. To solve this problem, our upsampling model, visualized in Figure 5, contains three components: a *reshape block*, n_u *upsample units* with the upsampling rate τ , and a *coordinate reconstruction block*.

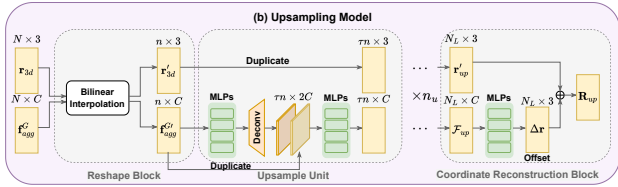


Figure 5. Point cloud upsampling module. Initially, the 3D radar points and their associated features are processed by a reshape block, yielding a fixed number of points. Subsequently, they pass through n_u upsample units, each upsampling the inputs by a factor of τ . Ultimately, point offsets are derived from the processed features within the coordinate reconstruction block.

Initially, radar points $\mathbf{r}_{3d} = \{(x_{3d}^j, y_{3d}^j, z_{3d}^j)\}_{j=1}^N$, along with their global features f_{agg}^G , are processed by the reshape block, employing bilinear interpolation to scale the data to a predetermined number of points $n = \frac{N_L}{\tau n_u}$. This generates a modified set of radar points $\mathbf{r}'_{3d} = \{(x_{3d}^{j'}, y_{3d}^{j'}, z_{3d}^{j'})\}_{j=1}^n$ and their associated features $f_{agg}^{G'} \in \mathbb{R}^{n \times C}$.

Inspired by [8], the process of our designed upsample unit involves duplicating the features τ times and concur-

rently processing them through a transposed convolutional layer to derive new point features. These resultant features are then concatenated along the channel axis and refined through two MLP layers. Simultaneously, the input points are replicated by a factor of τ .

Upon completing n_u upsample units, we derive the upsampled feature vectors $\mathcal{F}_{up} = \{f_{up}^j\}_{j=1}^{N_L}$ and the duplicated points $\mathbf{R}'_{up} = \{(X_{up}^{j'}, Y_{up}^{j'}, Z_{up}^{j'})\}_{j=1}^N$. The coordinate reconstruction block, utilizing \mathcal{F}_{up} as input, computes per-point offsets $\Delta \mathbf{r}$ through two MLPs. These offsets are subsequently added to the duplicated points, resulting in the final upsampled 3D point cloud \mathbf{R}_{up} .

This module returns two outputs, the upsampled point cloud \mathbf{R}_{up} and the upsampled features \mathcal{F}_{up} .

3.2.5 Feature refinement submodule.

This module augments the 2D features from two perspectives: utilizing aggregated features and incorporating upsampled features. Firstly, we enrich the 2D feature maps $\{F_{2d}^i\}_{i=1}^5$ by integrating the aggregated points features $\{f_{agg}^i\}_{i=1}^5$ at each respective scale i . More precisely, for the j^{th} point at the i^{th} scale, its feature is added back to the projected pixel coordinates $(\lfloor \frac{x_{2d}^j}{2^i} \rfloor, \lfloor \frac{y_{2d}^j}{2^i} \rfloor)$ on F_{2d}^i . In parallel, the global aggregated feature f_{agg}^G and the upsampled feature \mathcal{F}_{up} are projected onto the original, unscanned image plane served as a global feature map F_{2d}^0 . Specifically, for the j^{th} upsampled point $R_{up}^j = (X_{up}^j, Y_{up}^j, Z_{up}^j)$, it is mapped to 2D coordinates using the camera's intrinsic and its associated upsampled feature is stored into F_{2d}^0 . Importantly, any upsampled points in \mathbf{R}_{up} that fall outside the original image plane after projection is discarded.

Finally, we concatenate F_{2d}^0 with the refined $\{F_{2d}^i\}_{i=1}^5$, yielding six comprehensive radar feature maps, which are passed to the decoder for the depth estimation task. Additionally, the upsampled 3D points \mathbf{R}_{up} are output to facilitate loss calculation for this specific branch.

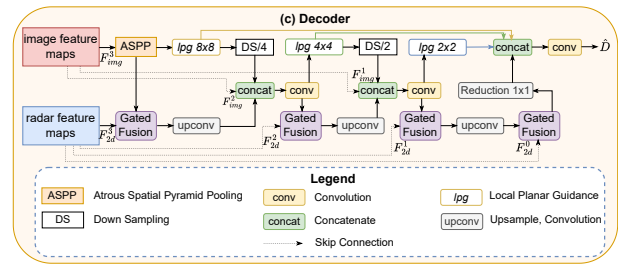


Figure 6. Decoder architecture for depth estimation.

3.3. Decoder

Our depth estimation framework is built upon the BTS model [19], leveraging the local planar guidance concept to enhance the upsampling process and extract more meaningful features. In this process, we incorporate both image features $\{F_{img}^i\}_{i=1}^5$ and radar features $\{F_{2d}^i\}_{i=0}^5$ as input

Table 1. Performance Comparison on nuScenes Official Test Set.

Eval Distance	Method	Sensors		Metrics							
		Image	Radar	MAE ↓	RMSE ↓	AbsRel ↓	log10 ↓	RMSElog ↓	δ_1 ↑	δ_2 ↑	δ_3 ↑
50m	BTS [19]	✓		1.937	3.885	0.116	0.045	0.179	0.883	0.957	1.937
	RC-PDA [26]	✓	✓	2.225	4.159	0.106	0.051	0.186	0.864	0.944	0.974
	RC-PDA-HG [26]	✓	✓	2.210	4.234	0.121	0.052	0.194	0.850	0.942	0.975
	DORN [24]	✓	✓	1.898	3.928	0.100	0.050	0.164	0.905	0.962	0.982
	RadarNet [37]	✓	✓	1.706	3.742	0.103	0.041	0.170	0.903	0.965	0.983
	CaFNet [40]	✓	✓	1.674	3.674	0.098	0.038	0.164	0.906	0.963	0.983
	Li <i>et al.</i> [20]	✓	✓	1.524	3.567	-	-	-	-	-	-
	GET-UP (Ours)	✓	✓	1.241	2.857	0.072	0.030	0.135	0.943	0.977	0.988
70m	BTS [19]	✓		2.346	4.811	0.119	0.047	0.188	0.872	0.952	0.979
	RC-PDA [26]	✓	✓	3.338	6.653	0.122	0.060	0.225	0.822	0.923	0.965
	RC-PDA-HG [26]	✓	✓	3.514	7.070	0.127	0.062	0.235	0.812	0.914	0.960
	DORN [24]	✓	✓	2.170	4.532	0.105	0.055	0.170	0.896	0.960	0.980
	RadarNet [37]	✓	✓	2.073	4.591	0.105	0.043	0.181	0.896	0.962	0.981
	CaFNet [40]	✓	✓	2.010	4.493	0.101	0.040	0.174	0.897	0.961	0.983
	Li <i>et al.</i> [20]	✓	✓	1.823	4.304	-	-	-	-	-	-
	GET-UP (Ours)	✓	✓	1.541	3.657	0.075	0.032	0.145	0.936	0.974	0.986
80m	BTS [19]	✓		2.467	5.125	0.120	0.048	0.191	0.869	0.951	0.979
	AdaBins [1]	✓		3.541	5.885	0.197	0.089	0.261	0.642	0.929	0.977
	P3Depth [32]	✓		3.130	5.838	0.165	0.065	0.222	0.804	0.934	0.974
	LapDepth [38]	✓		2.544	5.151	0.117	0.049	0.187	0.865	0.953	0.980
	S2D [†] [28]	✓	✓	2.374	5.628	0.115	-	-	0.876	0.949	0.974
	RC-PDA [26]	✓	✓	3.721	7.632	0.126	0.063	0.238	0.813	0.914	0.960
	RC-PDA-HG [26]	✓	✓	3.664	7.775	0.138	0.064	0.245	0.806	0.909	0.957
	DORN [24]	✓	✓	2.432	5.304	0.107	0.056	0.177	0.890	0.960	0.981
	RCDPT [†] [25]	✓	✓	-	5.165	0.095	-	-	0.901	0.961	0.981
	RadarNet [37]	✓	✓	2.179	4.899	0.106	0.044	0.184	0.894	0.959	0.980
	CaFNet [40]	✓	✓	2.109	4.765	0.101	0.040	0.176	0.895	0.959	0.981
	Li <i>et al.</i> [20]	✓	✓	1.927	4.610	-	-	-	-	-	-
GET-UP (Ours)	✓	✓	1.632	3.932	0.076	0.032	0.148	0.934	0.974	0.986	

[†] These results come from the paper that tests the model performance on a different test set. This leads to the metrics being less comparable.

and employ the gated fusion technique [37] to fuse radar and image features. Detailed visualizations of the decoder’s architecture are provided in Fig. 6.

3.4. Loss Functions

Our model employs two loss functions to facilitate depth estimation and point cloud upsampling tasks. To guide the depth estimation task, we follow methodologies from [37], accumulating LiDAR point clouds from neighboring frames to construct an accumulated depth map. Subsequently, we apply the scaffolding technique [48] to generate a dense depth map D . As demonstrated in [20], supervised by single scan depth D_s improves the depth prediction accuracy. Thus, we utilize D_s and D to supervise our depth estimation task as follows:

$$L_{Depth} = \frac{1}{|\Omega_s|} \sum_{x \in \Omega_s} |D_s(x) - \hat{D}(x)| + \frac{1}{|\Omega|} \sum_{x \in \Omega} |D(x) - \hat{D}(x)|, \quad (4)$$

which only calculated within the sets of pixels where D_s or D are valid.

The Chamfer distance loss [11] is utilized to reduce the discrepancy between the upsampled point cloud \mathbf{R}_{up} and

the ground truth \mathbf{R}_{gt} :

$$L_{Up} = \frac{1}{|\mathbf{R}_{up}|} \sum_{p \in \mathbf{R}_{up}} \min_{q \in \mathbf{R}_{gt}} \|p - q\|_2^2 + \frac{1}{|\mathbf{R}_{gt}|} \sum_{q \in \mathbf{R}_{gt}} \min_{p \in \mathbf{R}_{up}} \|p - q\|_2^2 \quad (5)$$

Here, p represents a 3D point in \mathbf{R}_{up} , and q denotes a 3D point in \mathbf{R}_{gt} . The term $\|\cdot\|_2^2$ signifies the squared Euclidean distance.

The final loss function is a weighted sum of the individual losses: $L = L_{Depth} + \alpha L_{Up}$, where α is a weighting factor to balance the importance of the two tasks.

4. Experiments

This section first introduces the dataset and the implementation details. Then, we describe the evaluation metrics and compare our GET-UP with the existing methodologies in the quantitative and qualitative aspects. Finally, we conduct ablation studies to further underscore our proposed methods’ effectiveness.

4.1. Dataset and Implementation Details

We utilize the nuScenes dataset [2], a comprehensive multi-sensor dataset dedicated to autonomous driving research, for the training and evaluation of our model. The

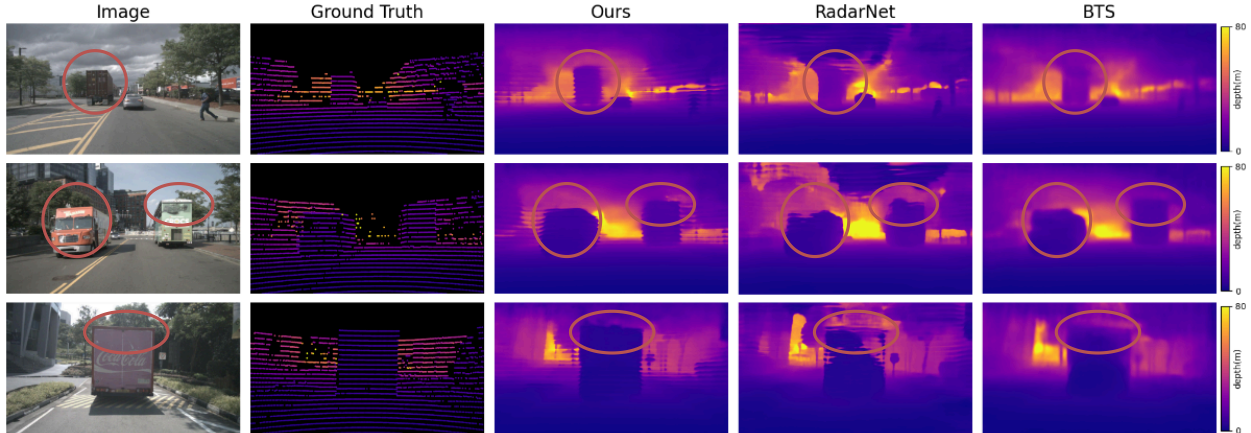


Figure 7. Qualitative comparison on nuScenes test set. Column 1 shows the RGB image; column 2 plots the ground truth depth map. We compare our result with the RadarNet and our baseline BTS at 80 meters depth range.

dataset is partitioned into training, validation, and test subsets, consisting of 700, 150, and 150 scenes, respectively. We utilize the front camera and radar data to train and evaluate our model. Notably, we employ a single radar scan as input and our model can handle undefined number of radar points as input.

For training, we aggregate 80 preceding and 80 succeeding LiDAR frames to create an accumulated depth map and then employ the scaffolding technique [48] to generate a dense depth map D . It’s important to note that for evaluation, the single-frame LiDAR depth map D_{gt} serves as the ground truth. In the point cloud upsampling task, we sample 128 LiDAR points per frame as the ground truth \mathbf{R}_{gt} , normalizing these points and the radar points using their centroid and maximum distance. The upsampled points estimated by the feature refinement submodule are then denormalized before projection onto the image plane.

Our model is developed in PyTorch [31] and trained on an Nvidia® Tesla A30 GPU with a batch size of 6. We employ the Adam optimizer [17] with an initial learning rate of $1e^{-4}$, adjusting it according to a polynomial decay rate with a power of $p = 0.9$. To prevent overfitting, image augmentation techniques such as random flips and adjustments to contrast, brightness, and color are applied. Moreover, random cropping to a size of 352×704 pixels is conducted during training to enhance the model robustness further.

4.2. Quantitative Results

In this study, we benchmark our GET-UP model against both image-based methods [1, 19, 32, 38] and existing radar-camera depth estimation approaches [20, 24–26, 37, 40], using the standard evaluation metrics, detailed in the supplementary material. The models are assessed on the official nuScenes test set across three evaluation ranges: up to 50 meters, 70 meters, and 80 meters, with detailed results presented in Table 1.

Our GET-UP model demonstrates superior performance over image-only methods across all metrics. Specifically, it enhances the BTS baseline [19] by 33.8% in MAE and 23.3% in RMSE, highlighting the substantial benefits of incorporating radar data into image-based methods. Furthermore, we explored LiDAR-camera depth completion techniques [28, 44] using radar data to generate sparse depth maps. These attempts yielded unsatisfactory outcomes due to the even sparser and more ambiguous nature of radar-generated depth maps. Techniques such as those in [5, 14, 52] prove inappropriate for radar-camera depth estimation tasks because they rely on a predetermined number of LiDAR points as inputs, which is incapable of handling various number of radar points.

Following the methodology of [37], our approach utilizes a single radar scan, contrasting with methods like [24–26] that employ multiple radar scans to enhance point cloud density. Remarkably, our method delivers superior results with fewer radar points compared to these approaches. Remarkably, GET-UP outperforms [20] by 18.6%, 18.3%, and 15.3% in MAE and 19.9%, 15.0%, and 14.7% in RMSE at the 50, 70, and 80-meter evaluation distances, respectively, demonstrating its efficacy in leveraging limited radar data for accurate depth estimation.

4.3. Qualitative Results

Fig. 7 showcases a comparative analysis of our GET-UP method against the baseline [19] and RadarNet [37]. Overall, our proposed GET-UP predicts depth maps with clearer object boundaries compared to RadarNet and the baseline, both at long and short ranges. For example, in the first row, GET-UP effectively distinguishes between the sky and the upper boundary of the track at a far distance. In the second and third rows, our method demonstrates greater robustness by accurately predicting the shapes of various objects.

4.4. Ablation Study

To further ascertain the efficiency of our GET-UP, we conduct a series of ablation studies to verify the effectiveness of each component. First, we analyze the impact of the ASCB. Secondly, the efficacy of the 3D feature extraction submodule is evaluated. At last, we quantify the reliability of the point cloud upsampling submodule.

4.4.1 Adaptive sparse convolution block.

Initially, we conducted experiments without utilizing any sparse convolution refinement, which directly extracts 2D features from radar projections. Subsequently, we compared our proposed ASCB against the conventional sparse convolution block [43], which employs a single mask alongside a sequence of kernel sizes set at [11, 7, 5, 3, 3]. Compared to the conventional sparse convolution block, our ASCB improves the RMSE with 7.7%.

Table 2. Ablation study on the sparse convolution block.

conventional [43]	ASCB	MAE ↓	RMSE ↓	AbsRel ↓	δ_1 ↑
✗	✗	1.852	4.432	0.093	0.909
✓	✗	1.792	4.262	0.088	0.918
✗	✓	1.632	3.932	0.076	0.934

4.4.2 Radar 3D feature extraction submodule.

In this section, we first conduct an experiment without 3D feature extraction. Thus, x_{Radar} is processed solely through the ASCB and then by the ResNet encoder. The result underscores the effectiveness of incorporating geometry information and the critical role of the 2D-3D feature aggregation and refinement process in enhancing model performance. Then, we benchmark our attention-enhanced DGCNN against established models such as GCN [18], GCN2 [4], and the original DGCNN [47] architectures. Furthermore, we explore the optimal number of nearest neighbors (k) for each radar point to determine the most effective value, with the comparative results presented in Table 3. The findings clearly demonstrate the superior performance of our attention-enhanced model. Notably, a larger k value degrades performance since it tends to only capture global features due to the sparse nature of radar points. This leads to errors during feature extraction, underscoring the importance of carefully selecting k to balance detail capture and noise minimization. Our proposed 3D feature extraction module improves the MAE by 6.5% compared to the solely 2D feature extraction architecture.

4.4.3 Point cloud upsampling submodule.

To demonstrate the effectiveness of this module, we initially perform an experiment excluding the upsampling task. Subsequently, we conduct further experiments to identify the optimal number of upsampling units n_u and the number of upsampled points N_L . All other components of the model remain unchanged during these evaluations. The results

Table 3. Ablation study on the GNN models.

Model	k-value	MAE ↓	RMSE ↓	REL ↓	δ_1 ↑
w/o GNN	N/A	1.884	4.663	0.090	0.911
GCN	3	1.877	4.432	0.087	0.918
GCN	4	1.852	4.401	0.085	0.921
GCN	6	1.882	4.441	0.088	0.917
GCN	8	1.894	4.485	0.087	0.918
GCN	10	1.896	4.489	0.089	0.916
GCN	4	1.852	4.401	0.085	0.921
GCN2	4	1.874	4.520	0.088	0.919
DGCNN	4	1.843	4.448	0.083	0.922
Ours	4	1.762	4.331	0.081	0.925

demonstrate that incorporating point cloud upsampling as an auxiliary task substantially enhances depth estimation accuracy. Moreover, given that the average count of radar points per frame is approximately 60, selecting an appropriate value for N_L is crucial to ensure the efficacy of the upsampling process.

Table 4. Ablation study on the upsampling module.

Upsampling	n_u	N_L	MAE ↓	RMSE ↓	REL ↓	δ_1 ↑
✗	N/A	N/A	1.762	4.331	0.081	0.925
✓	1	128	1.721	4.231	0.079	0.928
✓	2	128	1.632	3.932	0.076	0.934
✓	3	128	1.679	3.973	0.078	0.931
✓	2	64	1.702	4.090	0.080	0.929
✓	2	128	1.632	3.932	0.076	0.934
✓	2	256	1.683	3.969	0.077	0.932

5. Conclusion

In this paper, we propose GET-UP, a geometry-aware algorithm designed to tackle the significant challenges in radar-camera depth estimation due to the inherent ambiguity and sparsity of radar data. Our approach integrates both 2D and 3D representations of radar data, utilizing an attention-enhanced DGCNN model for the extraction of 3D features without compromising 2D spatial context. To address the issue of radar data sparsity, we implement two strategies: the ASCB, which densifies radar data on the 2D plane to facilitate the extraction of 2D features and a point cloud upsampling task that enhances radar point density from a 3D perspective. GET-UP sets a new benchmark on the nuScenes dataset, improving 15.3% in MAE and 14.7% in RMSE over the previously best-performing model. Looking ahead, exploring diverse upsampling algorithms on radar point clouds and refining the integration of 2D and 3D radar features present valuable directions for further research.

6. Acknowledgement

Research leading to these results has received funding from the EU ECSEL Joint Undertaking under grant agreement n° 101007326 (project AI4CSM) and from the partner national funding authorities the German Ministry of Education and Research (BMBF).

References

- [1] Shariq Farooq Bhat, Ibraheem Alhashim, and Peter Wonka. Adabins: Depth estimation using adaptive bins. In *Proceedings of the IEEE/CVF Conference on Computer Vision and Pattern Recognition*, pages 4009–4018, 2021. 1, 6, 7
- [2] Holger Caesar, Varun Bankiti, Alex H Lang, Sourabh Vora, Venice Erin Liong, Qiang Xu, Anush Krishnan, Yu Pan, Giancarlo Baldan, and Oscar Beijbom. nusenes: A multi-modal dataset for autonomous driving. In *Proceedings of the IEEE/CVF conference on computer vision and pattern recognition*, pages 11621–11631, 2020. 2, 5, 6
- [3] Simon Chadwick, Will Maddern, and Paul Newman. Distant vehicle detection using radar and vision. In *2019 International Conference on Robotics and Automation (ICRA)*, pages 8311–8317. IEEE, 2019. 1
- [4] Ming Chen, Zhewei Wei, Zengfeng Huang, Bolin Ding, and Yaliang Li. Simple and deep graph convolutional networks. In *International conference on machine learning*, pages 1725–1735. PMLR, 2020. 8
- [5] Yun Chen, Bin Yang, Ming Liang, and Raquel Urtasun. Learning joint 2d-3d representations for depth completion. In *Proceedings of the IEEE/CVF International Conference on Computer Vision*, pages 10023–10032, 2019. 2, 7
- [6] Xinjing Cheng, Peng Wang, and Ruigang Yang. Learning depth with convolutional spatial propagation network. *IEEE transactions on pattern analysis and machine intelligence*, 42(10):2361–2379, 2019. 1
- [7] Andrea Conti, Matteo Poggi, and Stefano Mattoccia. Sparsity agnostic depth completion. In *Proceedings of the IEEE/CVF Winter Conference on Applications of Computer Vision*, pages 5871–5880, 2023. 1, 2
- [8] Hang Du, Xuejun Yan, Jingjing Wang, Di Xie, and Shiliang Pu. Point cloud upsampling via cascaded refinement network. In *Proceedings of the Asian Conference on Computer Vision*, pages 586–601, 2022. 2, 5
- [9] David Eigen, Christian Puhrsch, and Rob Fergus. Depth map prediction from a single image using a multi-scale deep network. *Advances in neural information processing systems*, 27, 2014. 1
- [10] Abdelrahman Eldesokey, Michael Felsberg, and Fahad Shahbaz Khan. Confidence propagation through cnns for guided sparse depth regression. *IEEE transactions on pattern analysis and machine intelligence*, 42(10):2423–2436, 2019. 1
- [11] Haoqiang Fan, Hao Su, and Leonidas J Guibas. A point set generation network for 3d object reconstruction from a single image. In *Proceedings of the IEEE conference on computer vision and pattern recognition*, pages 605–613, 2017. 5, 6
- [12] Huan Fu, Mingming Gong, Chaohui Wang, Kayhan Batmanghelich, and Dacheng Tao. Deep ordinal regression network for monocular depth estimation. In *Proceedings of the IEEE conference on computer vision and pattern recognition*, pages 2002–2011, 2018. 1
- [13] Kaiming He, Xiangyu Zhang, Shaoqing Ren, and Jian Sun. Deep residual learning for image recognition. In *Proceedings of the IEEE conference on computer vision and pattern recognition*, pages 770–778, 2016. 2, 3
- [14] Lam Huynh, Phong Nguyen, Jiří Matas, Esa Rahtu, and Janne Heikkilä. Boosting monocular depth estimation with lightweight 3d point fusion. In *Proceedings of the IEEE/CVF International Conference on Computer Vision*, pages 12767–12776, 2021. 2, 7
- [15] Maximilian Jaritz, Raoul De Charette, Emilie Wirbel, Xavier Perrotton, and Fawzi Nashashibi. Sparse and dense data with cnns: Depth completion and semantic segmentation. In *2018 International Conference on 3D Vision (3DV)*, pages 52–60. IEEE, 2018. 1, 2
- [16] Vijay John and Seiichi Mita. Rvnet: Deep sensor fusion of monocular camera and radar for image-based obstacle detection in challenging environments. In *Image and Video Technology: 9th Pacific-Rim Symposium, PSIVT 2019, Sydney, NSW, Australia, November 18–22, 2019, Proceedings 9*, pages 351–364. Springer, 2019. 1
- [17] Diederik P. Kingma and Jimmy Ba. Adam: A method for stochastic optimization, 2017. 7
- [18] Thomas N Kipf and Max Welling. Semi-supervised classification with graph convolutional networks. *arXiv preprint arXiv:1609.02907*, 2016. 8
- [19] Jin Han Lee, Myung-Kyu Han, Dong Wook Ko, and Il Hong Suh. From big to small: Multi-scale local planar guidance for monocular depth estimation. *arXiv preprint arXiv:1907.10326*, 2019. 1, 3, 5, 6, 7
- [20] Huadong Li, Minhao Jing, Jiajun Liang, Haoqiang Fan, and Renhe Ji. Sparse beats dense: Rethinking supervision in radar-camera depth completion. *arXiv preprint arXiv:2312.00844*, 2023. 2, 6, 7
- [21] Ruihui Li, Xianzhi Li, Chi-Wing Fu, Daniel Cohen-Or, and Pheng-Ann Heng. Pu-gan: a point cloud upsampling adversarial network. In *Proceedings of the IEEE/CVF international conference on computer vision*, pages 7203–7212, 2019. 2
- [22] Zhenyu Li, Xuyang Wang, Xianming Liu, and Junjun Jiang. Binsformer: Revisiting adaptive bins for monocular depth estimation. *arXiv preprint arXiv:2204.00987*, 2022. 1
- [23] Juan-Ting Lin, Dengxin Dai, and Luc Van Gool. Depth estimation from monocular images and sparse radar data. In *2020 IEEE/RSJ International Conference on Intelligent Robots and Systems (IROS)*, pages 10233–10240. IEEE, 2020. 2
- [24] Chen-Chou Lo and Patrick Vandewalle. Depth estimation from monocular images and sparse radar using deep ordinal regression network. In *2021 IEEE International Conference on Image Processing (ICIP)*, pages 3343–3347. IEEE, 2021. 1, 2, 6, 7
- [25] Chen-Chou Lo and Patrick Vandewalle. Rcdpt: Radar-camera fusion dense prediction transformer. In *ICASSP 2023 - 2023 IEEE International Conference on Acoustics, Speech and Signal Processing (ICASSP)*, pages 1–5, 2023. 6, 7
- [26] Yunfei Long, Daniel Morris, Xiaoming Liu, Marcos Castro, Punarjay Chakravarty, and Praveen Narayanan. Radar-camera pixel depth association for depth completion. In *Proceedings of the IEEE/CVF Conference on Computer Vision and Pattern Recognition*, pages 12507–12516, 2021. 1, 2, 6, 7

- [27] Luqing Luo, Lulu Tang, Wanyi Zhou, Shizheng Wang, and Zhi-Xin Yang. Pu-eva: An edge-vector based approximation solution for flexible-scale point cloud upsampling. In *Proceedings of the IEEE/CVF International Conference on Computer Vision*, pages 16208–16217, 2021. 2
- [28] Fangchang Ma and Sertac Karaman. Sparse-to-dense: Depth prediction from sparse depth samples and a single image. In *2018 IEEE international conference on robotics and automation (ICRA)*, pages 4796–4803. IEEE, 2018. 1, 2, 6, 7
- [29] Felix Nobis, Maximilian Geisslinger, Markus Weber, Johannes Betz, and Markus Lienkamp. A deep learning-based radar and camera sensor fusion architecture for object detection. In *2019 Sensor Data Fusion: Trends, Solutions, Applications (SDF)*, pages 1–7. IEEE, 2019. 1
- [30] Jinsun Park, Kyungdon Joo, Zhe Hu, Chi-Kuei Liu, and In So Kweon. Non-local spatial propagation network for depth completion. In *Computer Vision—ECCV 2020: 16th European Conference, Glasgow, UK, August 23–28, 2020, Proceedings, Part XIII 16*, pages 120–136. Springer, 2020. 1, 2
- [31] Adam Paszke, Sam Gross, Francisco Massa, Adam Lerer, James Bradbury, Gregory Chanan, Trevor Killeen, Zeming Lin, Natalia Gimelshein, Luca Antiga, Alban Desmaison, Andreas Köpf, Edward Yang, Zach DeVito, Martin Raison, Alykhan Tejani, Sasank Chilamkurthy, Benoit Steiner, Lu Fang, Junjie Bai, and Soumith Chintala. Pytorch: An imperative style, high-performance deep learning library. *ArXiv*, abs/1912.01703, 2019. 7
- [32] Vaishakh Patil, Christos Sakaridis, Alexander Liniger, and Luc Van Gool. P3depth: Monocular depth estimation with a piecewise planarity prior. In *Proceedings of the IEEE/CVF Conference on Computer Vision and Pattern Recognition*, pages 1610–1621, 2022. 1, 6, 7
- [33] Guocheng Qian, Abdulellah Abualshour, Guohao Li, Ali Thabet, and Bernard Ghanem. Pu-gcn: Point cloud upsampling using graph convolutional networks. In *Proceedings of the IEEE/CVF Conference on Computer Vision and Pattern Recognition*, pages 11683–11692, 2021. 2, 5
- [34] Jiaxiong Qiu, Zhaopeng Cui, Yinda Zhang, Xingdi Zhang, Shuaicheng Liu, Bing Zeng, and Marc Pollefeys. DeepLidar: Deep surface normal guided depth prediction for outdoor scene from sparse lidar data and single color image. In *Proceedings of the IEEE/CVF Conference on Computer Vision and Pattern Recognition*, pages 3313–3322, 2019. 1
- [35] Ashutosh Saxena, Sung Chung, and Andrew Ng. Learning depth from single monocular images. *Advances in neural information processing systems*, 18, 2005. 1
- [36] Ashutosh Saxena, Min Sun, and Andrew Y Ng. Make3d: Learning 3d scene structure from a single still image. *IEEE transactions on pattern analysis and machine intelligence*, 31(5):824–840, 2008. 1
- [37] Akash Deep Singh, Yunhao Ba, Ankur Sarker, Howard Zhang, Achuta Kadambi, Stefano Soatto, Mani Srivastava, and Alex Wong. Depth estimation from camera image and mmwave radar point cloud. In *Proceedings of the IEEE/CVF Conference on Computer Vision and Pattern Recognition*, pages 9275–9285, 2023. 1, 2, 3, 6, 7
- [38] Minsoo Song, Seokjae Lim, and Wonjun Kim. Monocular depth estimation using laplacian pyramid-based depth residuals. *IEEE Transactions on Circuits and Systems for Video Technology*, 31(11):4381–4393, 2021. 6, 7
- [39] Huawei Sun, Hao Feng, Gianfranco Mauro, Julius Ott, Georg Stettinger, Lorenzo Servadei, and Robert Wille. Enhanced radar perception via multi-task learning: Towards refined data for sensor fusion applications. In *2024 IEEE Intelligent Vehicles Symposium (IV)*, pages 3179–3184, 2024. 1
- [40] Huawei Sun, Hao Feng, Julius Ott, Lorenzo Servadei, and Robert Wille. Cafnet: A confidence-driven framework for radar camera depth estimation. *arXiv preprint arXiv:2407.00697*, 2024. 1, 2, 6, 7
- [41] Huawei Sun, Hao Feng, Georg Stettinger, Lorenzo Servadei, and Robert Wille. Multi-task cross-modality attention-fusion for 2d object detection. In *2023 IEEE 26th International Conference on Intelligent Transportation Systems (ITSC)*, pages 3619–3626, 2023. 1
- [42] Jie Tang, Fei-Peng Tian, Wei Feng, Jian Li, and Ping Tan. Learning guided convolutional network for depth completion. *IEEE Transactions on Image Processing*, 30:1116–1129, 2020. 1, 2
- [43] Jonas Uhrig, Nick Schneider, Lukas Schneider, Uwe Franke, Thomas Brox, and Andreas Geiger. Sparsity invariant cnns. In *2017 international conference on 3D Vision (3DV)*, pages 11–20. IEEE, 2017. 4, 8
- [44] Wouter Van Gansbeke, Davy Neven, Bert De Brabandere, and Luc Van Gool. Sparse and noisy lidar completion with rgb guidance and uncertainty. In *2019 16th international conference on machine vision applications (MVA)*, pages 1–6. IEEE, 2019. 7
- [45] Ashish Vaswani, Noam Shazeer, Niki Parmar, Jakob Uszkoreit, Llion Jones, Aidan N Gomez, Łukasz Kaiser, and Illia Polosukhin. Attention is all you need. *Advances in neural information processing systems*, 30, 2017. 4
- [46] Xiaoyan Wang, Chunping Hou, Liangzhou Pu, and Yonghong Hou. A depth estimating method from a single image using foe crf. *Multimedia Tools and Applications*, 74:9491–9506, 2015. 1
- [47] Yue Wang, Yongbin Sun, Ziwei Liu, Sanjay E Sarma, Michael M Bronstein, and Justin M Solomon. Dynamic graph cnn for learning on point clouds. *ACM Transactions on Graphics (tog)*, 38(5):1–12, 2019. 4, 8
- [48] Alex Wong, Xiaohan Fei, Stephanie Tsuei, and Stefano Soatto. Unsupervised depth completion from visual inertial odometry. *IEEE Robotics and Automation Letters*, 5(2):1899–1906, 2020. 6, 7
- [49] Xin Xiong, Haipeng Xiong, Ke Xian, Chen Zhao, Zhiguo Cao, and Xin Li. Sparse-to-dense depth completion revisited: Sampling strategy and graph construction. In *Computer Vision—ECCV 2020: 16th European Conference, Glasgow, UK, August 23–28, 2020, Proceedings, Part XXI 16*, pages 682–699. Springer, 2020. 2
- [50] Yanchao Yang, Alex Wong, and Stefano Soatto. Dense depth posterior (ddp) from single image and sparse range. In *Proceedings of the IEEE/CVF Conference on Computer Vision and Pattern Recognition (CVPR)*, June 2019. 1, 2

- [51] Lequan Yu, Xianzhi Li, Chi-Wing Fu, Daniel Cohen-Or, and Pheng-Ann Heng. Pu-net: Point cloud upsampling network. In *Proceedings of the IEEE conference on computer vision and pattern recognition*, pages 2790–2799, 2018. [2](#)
- [52] Zhu Yu, Zehua Sheng, Zili Zhou, Lun Luo, Si-Yuan Cao, Hong Gu, Huaqi Zhang, and Hui-Liang Shen. Aggregating feature point cloud for depth completion. In *Proceedings of the IEEE/CVF International Conference on Computer Vision*, pages 8732–8743, 2023. [2](#), [7](#)
- [53] Shanshan Zhao, Mingming Gong, Huan Fu, and Dacheng Tao. Adaptive context-aware multi-modal network for depth completion. *IEEE Transactions on Image Processing*, 30:5264–5276, 2021. [2](#)